Retina

Three-Dimensional Volume Calculation of Intrachoroidal Cavitation Using Deep-Learning–Based Noise Reduction of Optical Coherence Tomography

Satoko Fujimoto[1,2], Atsuya Miki[1,3], Kazuichi Maruyama[1,4], Song Mei[5], Zaixing Mao[5], Zhenguo Wang[5], Kinpui Chan[5], and Kohji Nishida[1,6]

[1] Department of Ophthalmology, Graduate School of Medicine, Osaka University, Osaka, Japan
[2] Hawaii Macula and Retina Institute, Aiea, HI, USA
[3] Department of Myopia Control Research, Aichi Medical University Medical School, Aichi, Japan
[4] Department of Vision Informatics, Osaka University Graduate School of Medicine, Osaka, Japan
[5] Topcon Advanced Biomedical Imaging Laboratory, Oakland, NJ, USA
[6] Integrated Frontier Research for Medical Science Division, Institute for Open and Transdisciplinary Research Initiatives, Osaka University, Osaka, Japan

Correspondence: Atsuya Miki, Department of Myopia Control Research, Aichi Medical University Medical School, 1-1 Yazakokarimata, Nagakute, Aichi 480-1195, Japan. e-mail: a.miki.md@gmail.com

Purpose: Intrachoroidal cavitations (ICCs) are peripapillary pathological lesions generally associated with high myopia that can cause visual field (VF) defects. The current study aimed to evaluate a three-dimensional (3D) volume parameter of ICCs segmented from volumetric swept-source optical coherence tomography (SS-OCT) images processed using deep learning (DL)-based noise reduction and to investigate its correlation with VF sensitivity.

Methods: Thirteen eyes of 12 consecutive patients with peripapillary ICCs were enrolled. DL-based denoising and further analyses were applied to parapapillary 6 × 6-mm volumetric SS-OCT scans. Then, 3D ICC volume and two-dimensional depth and length measurements of the ICCs were calculated. The correlations between ICC parameters and VF sensitivity were investigated.

Results: The ICCs were located in the inferior hemiretina in all eyes. ICC volume ($P = 0.02$; regression coefficient [RC], -0.007) and ICC length ($P = 0.04$; RC, -4.51) were negatively correlated with the VF mean deviation, whereas ICC depth ($P = 0.15$) was not. All of the parameters, including ICC volume ($P = 0.01$; RC, -0.004), ICC depth ($P = 0.02$; RC, -0.008), and ICC length ($P = 0.045$; RC, -2.11), were negatively correlated with the superior mean total deviation.

Conclusions: We established the volume of ICCs as a new 3D parameter, and it reflected their influence on visual function. The automatic delineation and 3D rendering may lead to improved detection and pathological understanding of ICCs.

Translational Relevance: This study demonstrated the correlation between the 3D volume of ICCs and VF sensitivity.

Introduction

Intrachoroidal cavitations (ICCs), originally referred to as peripapillary detachments in pathologic myopia, are peripapillary pathological lesions associated with myopia that generally are located inferior to the myopic conus or parapapillary atrophy.[1,2] Later optical coherence tomography (OCT) studies showed that ICCs are intrachoroidal hyporeflective spaces, and as a result they were referred to as ICCs.[3,4]

ICCs are relatively common in myopic eyes. Shimada et al.[2] reported that ICCs occurred in 4.9% of highly myopic eyes. Choudhury and colleagues[5]

reported that the prevalence of ICCs evaluated by fundus photography was as high as 2.2% in Chinese subjects 50 years and older. The actual prevalence of ICCs could be even higher than in that photographic evaluation, because the typical yellow–orange lesions on fundus photographs were found in only 53% of eyes with ICCs.[6] In addition, ICCs can cause serious clinical consequences such as visual field (VF) defects.[2,7-9] Spaide et al.[10] reported a full-thickness retinal defect over the ICC or a herniation of the overlying retina into the ICC space, which might damage the corresponding course of nerve fiber and cause VF defects.

Although ICCs are relatively common, often with significant clinical consequences, many important characteristics of ICCs, including the pathogenesis, visual consequences, longitudinal changes, and risk factors, are not fully understood, possibly because most previous studies relied on two-dimensional (2D) (cross-sectional) OCT scans to evaluate ICC morphology. The existing 2D metrics of ICCs, such as depth and length,[6] do not fully capture the complex three-dimensional (3D) morphologic characteristics. Quantitative 3D OCT analyses of ICCs are unavailable in clinical practice mainly because of limitations in the imaging technology. In particular, a noise reduction technique is necessary to accurately delineate the borders of ICCs. However, multiple image averaging, which is the most common approach for reducing speckle noise, is limited to the use of 2D scans because this technique significantly increases the scan time. An alternative approach for noise reduction that does not increase scan time is needed to develop 3D evaluation capabilities of these lesions.

Recently, the benefits of deep learning (DL) have been reported for automated screening of clinical diseases[11–13] and automated segmentation of OCT.[14–17] We previously developed a method of DL-based noise reduction and 3D rendering of volumetric swept-source OCT (SS-OCT) images.[18] This technique can achieve image quality comparable to $128\times$ image averaging without extending the scan time.[18,19] Using this technique, we conducted automated delineation and 3D rendering of ICCs. We calculated the 3D (volume) and 2D (depth and length) metrics of ICCs from the 3D-rendered images of ICCs and investigated the correlation between these parameters and the baseline clinical characteristics including VF sensitivity. We also investigated the spatial relationship between ICCs and the optic nerve head (ONH) by overlaying the Bruch's membrane opening (BMO) images on the ICC images.

Methods

Study Participants

The current study included consecutive patients with peripapillary ICCs who underwent SS-OCT imaging from January 2018 to June 30, 2020, at the Department of Ophthalmology, Osaka University Hospital. All participants underwent a complete ocular examination, including autorefractometry (ARK-530; Nidek, Aichi, Japan), measurement of the axial length (AL) using the IOLMaster (Carl Zeiss Meditec, Jena, Germany), measurement of intraocular pressure (IOP), slit-lamp biomicroscopy, Swedish interactive threshold algorithm standard 30-2 or 24-2 VF tests (Humphrey Field Analyzer; Carl Zeiss Meditec), dilated fundus examinations, and color fundus photography (TRC-50DX; Topcon, Tokyo, Japan). Mean deviation (MD) and mean total deviation of the corresponding hemifield (i.e., superior hemifield for inferior ICCs) were obtained as VF sensitivity measures. The optic disc ovality index (the ratio of the shortest optic disc diameter to the longest disc diameter) was calculated from the fundus photographs[20–22] using ImageJ 1.53e (National Institutes of Health, Bethesda, MD). The exclusion criteria included extremely large ICCs that protruded from the 6×6-mm^2 OCT volume scans. The institutional review board (IRB) of Osaka University Hospital approved the study protocol, which adhered to the tenets of the Declaration of Helsinki. The IRB waived the need for written informed consent because of the non-invasive and retrospective nature of the study.

SS-OCT Imaging/Image Processing

A commercially available SS-OCT device, DRI OCT (Topcon), was used to image the peripapillary area with 6×6-mm2 volume scans. The center wavelength is 1050 nm, and the scanning speed is 100,000 axial scans per second. Eyes were imaged using the 3D scan mode, of which the A-scan density was 512 lines (horizontal) $\times$ 256 lines (vertical), within the scan time of 1.3 seconds.

Figure 1A shows the flowchart for 3D ICC detection. The ICC regions were defined where the posterior bowing of the sclera could be seen beneath the retina, referring to the report from Spaide and coworkers.[10] The OCT volumes were processed using a DL-based noise reduction algorithm and shadow reduction algorithm. These algorithms were the same as published previously.[18] Briefly, for DL-based denoising, we used two repeated B-scan frames at the
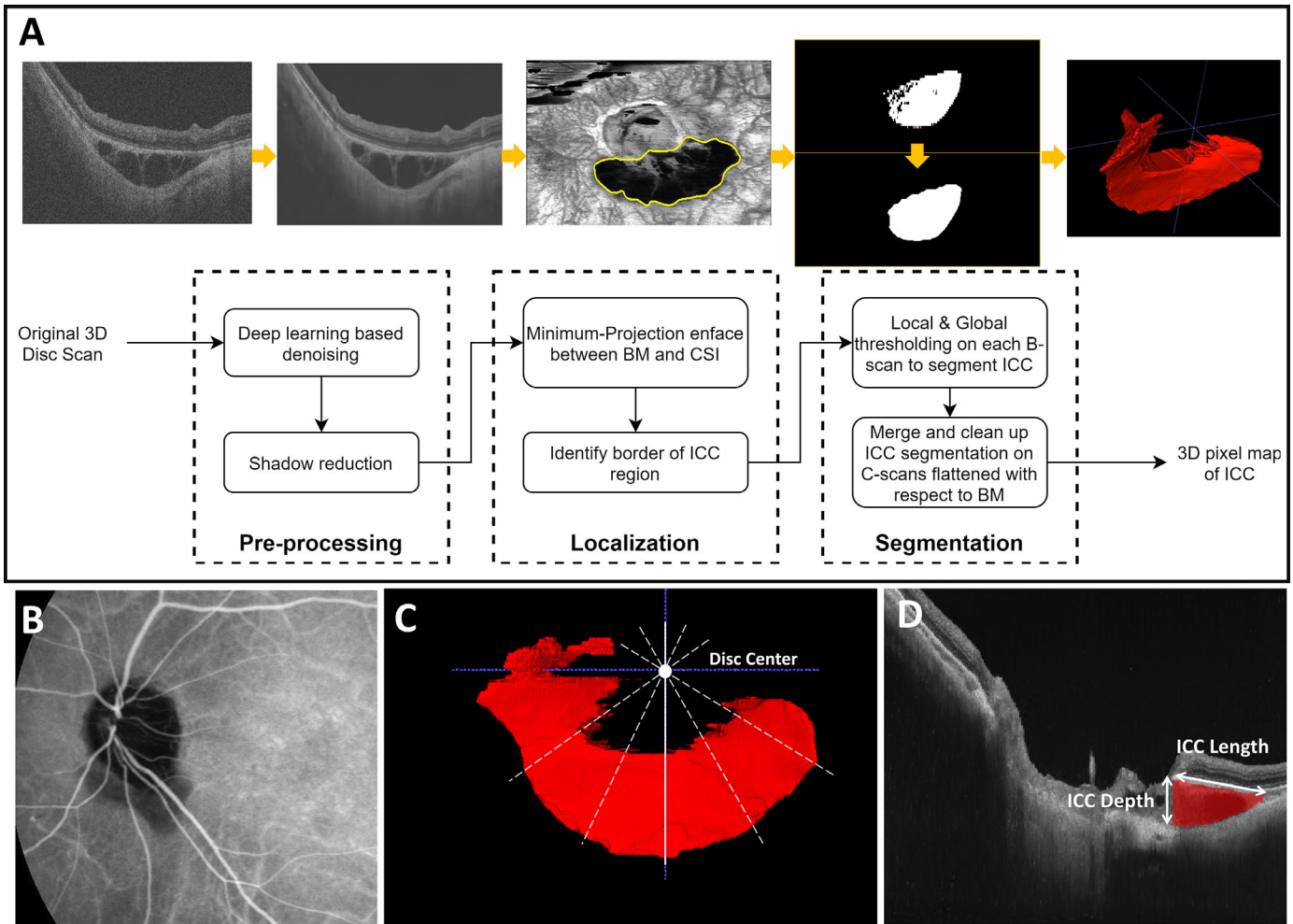
Figure 1. (A) The flowchart for 3D ICC detection. CSI, choroidal–sclera interface. (B) A late-phase indocyanine green angiography image of an ICC; no blood flow can be seen in the ICC. (C) An image of the measurement of 2D parameters of ICCs by every 30° (*dotted* and *continuous white lines*) around the disc center. (D) A B-scan image of the *continuous white line* in (C). ICC depth and length were measured at each location.

same location as training input, and the algorithm learns to keep the consistent structure and reduce the variance. The shadow reduction is based on a concept that a shadow corresponds to a reduction in the cumulated energy along its A-line. We passed the energy profile through a low-pass filter that removes the high-frequency components and rescales the A-lines based on the filtered energy profile, effectively compensating for the shadows without changing other regions. The high-frequency components removed in the profile correspond to noise and shadow, and the low-frequency components remaining correspond to the underlying structure. Therefore, the method can reduce the shadow without changing the structure.

After preprocessing, a minimum-projection en face image of the scan was generated from the slab between the BM and the choroidal–sclera interface. The chorioretinal segmentation was obtained using the built-in software for FastMap, the Topcon commercial SS-OCT system, and the hyporeflective nature of ICCs facilitates their localization based on the en face image intensity. Morphologic operations were applied to the localized region to smooth the boundary and fill in the holes internally. After localization, the ICCs were segmented on each B-scan within the ICC region previously defined on the en face images. ICCs have not been histologically investigated yet, and it has not been established how to define the boundaries of ICCs. We confirmed that the homogeneous remains within the cavitation had hypofluorescence and hypovascularity by indocyanine green angiography (Fig. 1B). Therefore, in this study, they were included in the measurement of ICC volume so as to calculate the whole

cavitation. The B-scan images were linearly scaled to remove the background and enhance the contrast in the retinal structure. Both the Niblack local thresholding[2] method and a global thresholding method with a fixed threshold were used to segment the ICC region, and each result was obtained by combining the two detected regions. After detecting the ICCs on the B-scan images, the segmentation results were postprocessed along the C-scan direction and flattened with respect to BM. Based on the notion that ICCs should be connected and smooth in the C-scan direction, the segmentation was merged and cleaned for optimization. Supplementary Figure S1 shows comparisons between the original B-scans and the denoised B-scans with segmentations.

We obtained a 3D map of the ICC region after segmentation and imported it into the free open-source image processing software ITK-SNAP 3.8.0 (www.itksnap.org.)[23] to render and observe the ICC structure. Because the software allows an overlaid display of the image and segmentation, the ICC segmentation also was inspected and corrected as needed.

ICC volume was calculated directly from the 3D map by multiplying the number of voxels corresponding to the ICC region by the voxel resolution defined by the OCT device. Each voxel resolution was calculated from the product of the pixel resolution along all three dimensions. The transverse resolutions were calculated from the ratio between the physical scan length (6 mm horizontal, 6 mm vertical) and the number of A-lines along each direction (512 horizontal, 256 vertical). The z (depth) resolution was determined by the system and extracted from the scan data (2.6 μm/pixel). We exported these results and performed all the quantitative calculation in MATLAB (MathWorks, Natick, MA).

We also measured the ICC depth and length as 2D parameters as reported previously.[6,24] The disc center was defined as the centroid of the BMO boundary. The ICC depth was measured at the deepest location in the interpolated scans along every 30°. The ICC length was measured along every 30° (covered by the ICC) around the disc center defined by the BMO. We also used MATLAB for this calculation. The maximum depths and lengths were used for the analyses. Figures 1C and 1D show images of the measurement of the ICC depth and length.

To evaluate the spatial relationship between ICCs and ONH, we also segmented the BMO (OCT-defined border of the ONH) from the preprocessed volume with a DL-based method published previously.[18] Supplementary Figure S2 shows the flowchart. Briefly, a rough disc segmentation was obtained from the en face image by thresholding. The volume was interpolated into 180 radial scans passing through the center of the disc. A patch of the interpolated B-scan centered at the crossing point between BM and the rough disc segmentation was used as input for the DL model. The predicted BMO locations were converted back to the coordinates of the volume scan. The BMO algorithm was validated internally on 194 scans, with an overall detection accuracy of 96%. Due to the highly challenging BMO segmentation at the location of the ICC, the detected BMO points were inspected manually and corrected as needed for optimization. Because the BMO and ICC were segmented from the same OCT volume, they were co-localized, and their location was overlaid without the need for registration. We created anatomic relation maps using en face ICC and BMO images that show the overlay of the optic disc and ICC.

Statistical Analysis

Descriptive statistics such as the mean, standard deviation (SD), and range were computed for each variable. Linear regression analyses were performed to explore correlations among each ICC metric (volume, depth, and length) and clinical factors such as VF sensitivity (MD and mean total deviation), optic disc tilt index, age, AL, spherical equivalent, and IOP. All statistical analyses were performed using JMP Pro 13.2.1 (SAS Institute, Cary, NC). A *P* value less than 0.05 was considered statistically significant.

Results

Thirteen eyes of 12 subjects (five men, seven women; mean ± SD age, 52.5 ± 6.3 years; range, 40–61) were included in the analysis. The parameters evaluated were the mean refractive error (−8.4 ± 3.2 diopters [D]; range, −2.75 to −14.5), AL (27.1 ± 1.4 mm; range, 24.49–30.05), IOP (13.6 ± 2.8 mmHg; range, 11–17.5), and optic disc ovality index (1.30 ± 0.18; range, 1.10–1.83). No subjects had pathological myopia according to the International Photographic Classification and Grading System for Myopic Maculopathy.[25]

Seven eyes had abnormal VFs (54%), with visual field median deviations (VFMDs) that ranged from −11.1 to 0.12 decibels (dB) (mean ± SD, −2.61 ± 3.16 dB). Five eyes had superior VF defects only, one had both superior and inferior VF defects, and one had inferior VF defects only. Eight eyes had enlarged Marriott blind spots, which indicate the influence of
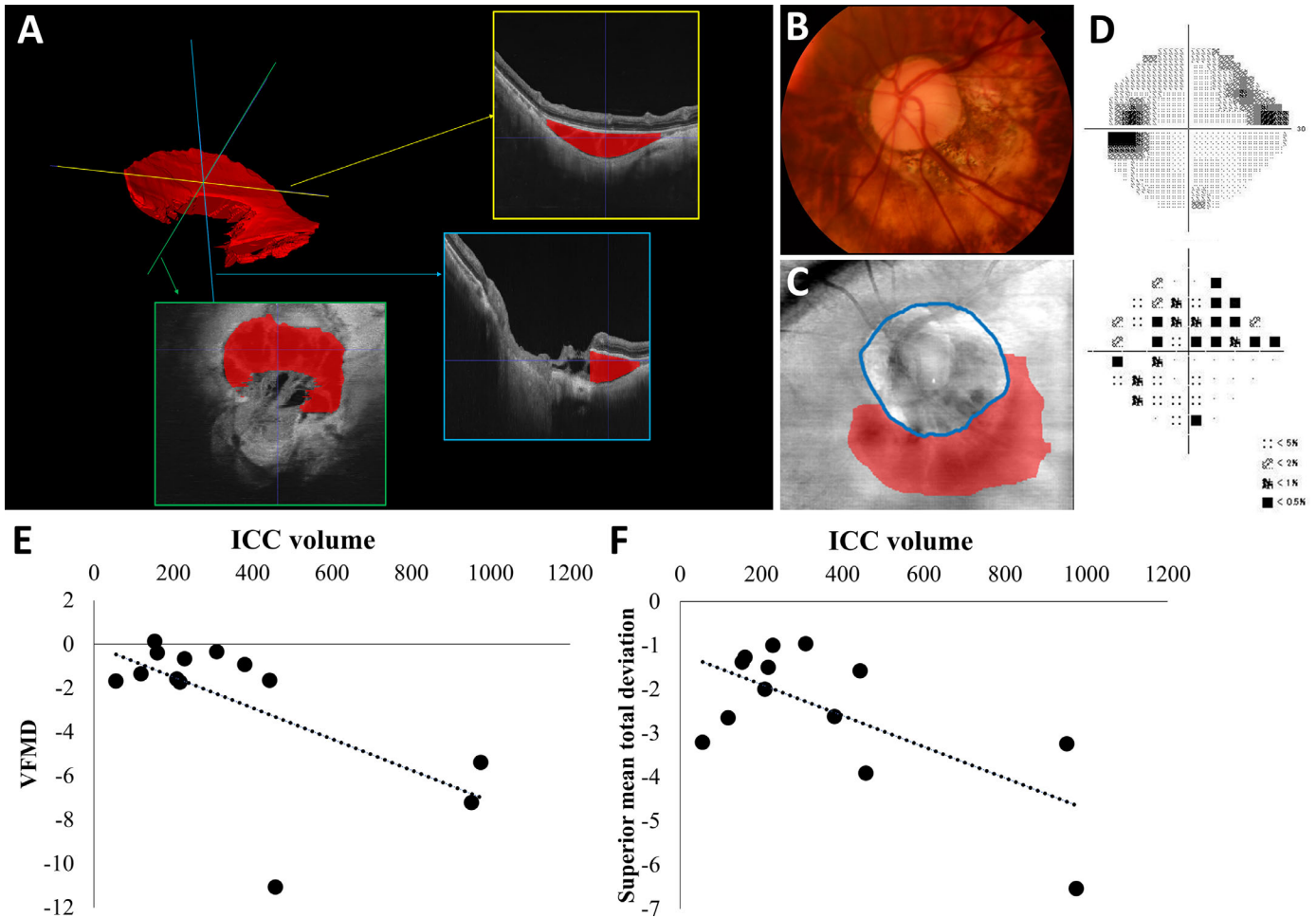
Figure 2. (A) Representative 3D image of an ICC. (B) Fundus photograph. (C) Schema of the spatial relationship between ICCs and the edge of the BMO (the *blue circle* indicates the edge of the BMO, and the *red zone* indicates the ICC zone). (D) *Upper image* shows the visual field defect, and the *lower image* shows total deviation. (E) Data distribution plots between ICC volume and VFMD. ICC volume was correlated negatively with VFMD. (F) Data distribution plots between ICC volume and the superior mean total deviation. ICC volume was correlated negatively with the superior mean total deviation.

large parapapillary atrophy, and three of the eight eyes had no other VF defects than enlarged Marriott blind spots. OCT detected inferior nerve fiber layer (NFL) defects in all eyes. Inner retinal defects over the ICCs were not seen in the subjects. The herniations of the nerve tissue into the ICCs were detected in eight of 13 eyes, and two eyes had VF defects in spite of neither herniation nor inner retinal defects. Fundus photographs showed parapapillary atrophy alpha (with irregular retinal pigmental epithelium [RPE]), beta (with BM and without RPE), and gamma (without BM or RPE) zones in all eyes. The Table shows the baseline characteristics of the participants.

The ICCs were in the inferior sector of the ONH in all 13 eyes (100%); one subject had bilateral ICCs. A typical photographic yellow–orange lesion inferior to

the peripapillary atrophy beta zone was found in 12 of the 13 eyes (92%).

The ICCs were segmented and visualized successfully in 3D in all eyes. Figure 2A and Supplementary Movie S1 show a representative case of 3D ICC, and the correlating fundus photograph, ICC–ONH overlay image, and visual field defect are shown in Figures 2B, 2C, and 2D, respectively. The mean ICC volume was $358.4 \pm 283.3 \times 10^{-3}$ mm^3 (range, 55.3–975.4), the mean ICC depth was 248.5 ± 108.9 μm (range, 118.5–512.4), and the mean ICC length was 1138.7 ± 396.9 μm (range, 416.3–2000.5). ICC volume was correlated positively with the depth ($P <$ 0.0001; regression coefficient [RC], 2.5) and length (P = 0.0002; RC, 610.7). ICC volume ($P = 0.02$; RC, -0.007) and ICC length ($P = 0.04$; RC, -4.51) were

Table. Baseline Characteristics and Correlation With ICC Volume

| Characteristic	Mean (SD)	Standardized Coefficient	*P*
Age (y)	52.5 (6.3)	−0.003	0.95
Refractive error (D)	−8.4 (3.2)	−0.34	0.26
Axial length (mm)	27.1 (1.4)	0.53	0.0611
Intraocular pressure (mmHg)	13.6 (2.8)	0.037	0.91
Optic disc ovality index	1.30 (0.18)	−0.30	0.32
Humphrey field analyzer medial division (dB)	−2.61 (3.16)	−0.64	0.0197[a]

[a] $P < 0.05$.
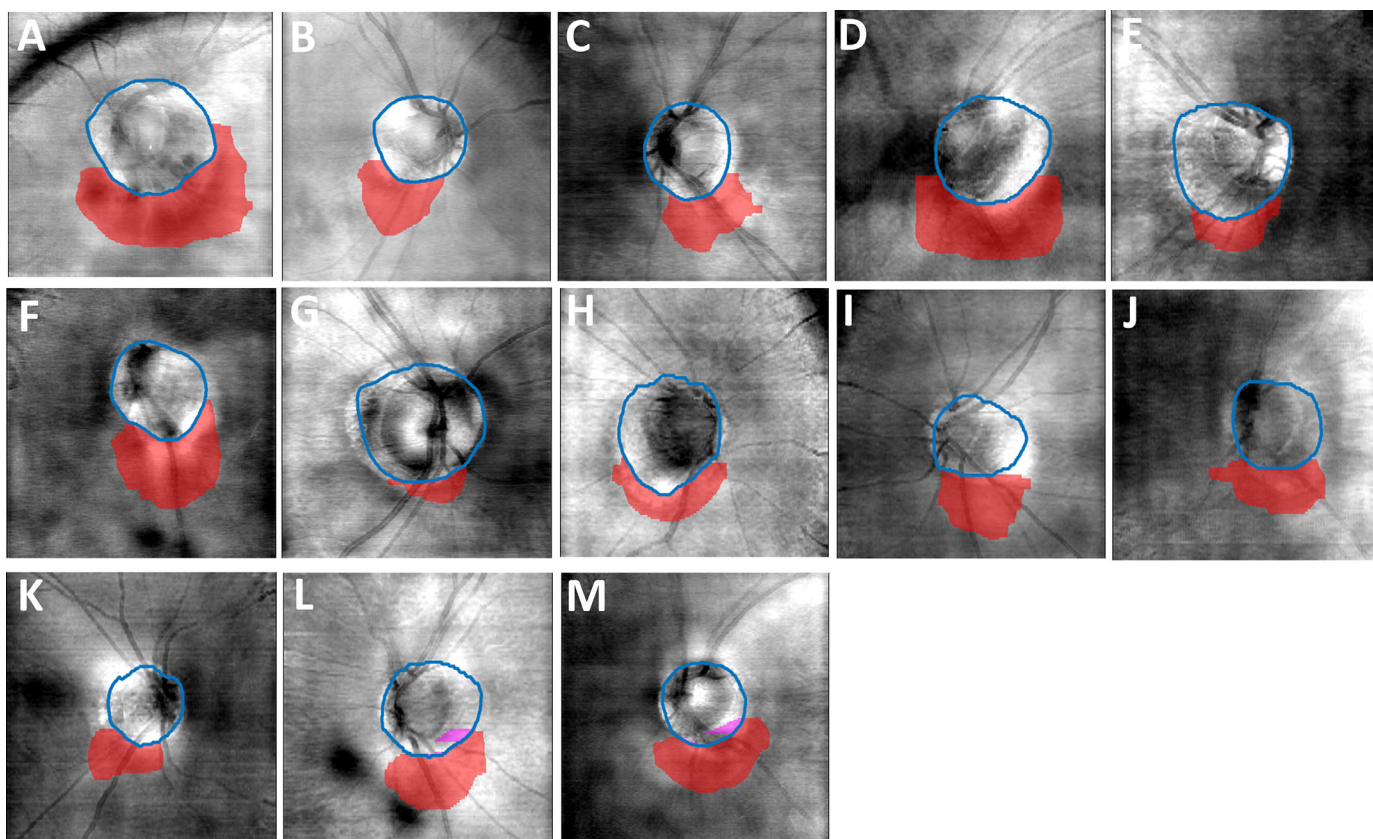
Figure 3. All 13 overlay images between ICCs and ONHs. (A–M) All ICCs are in direct contact with the edges of the BMO. (L) and (M) show two of the 13 cases that had overlap between ICCs and ONHs. The *blue circles* indicate the edges of the BMO, the *red zones* indicate the ICC zones, and the *pink zones* indicate the ONH–ICC overlay zone.

correlated negatively with the VFMD, whereas ICC depth ($P = 0.15$; RC, −0.012) was not. All of the ICC metrics, including ICC volume ($P = 0.01$; RC, −0.004), ICC depth ($P = 0.02$; RC, −0.008), and ICC length ($P = 0.045$; RC, 2.11), were correlated negatively with the superior mean total deviation. Figure 2E shows the data distribution plots between ICC volume and VFMD, and Figure 2F shows the plots between ICC volume and the superior mean total deviation.

ICC volume was not correlated significantly with other baseline factors such as age, refractive error, IOP, optic disc ovality index, or AL (Table).

On anatomic relation maps using en face ICC and BMO images, all of the ICCs had direct contact with the BMO edges, and the ICC and ONH overlapped each other in two cases (Fig. 3). The representative cases with direct contact between the BMO edges and ICC with and without en face overlay
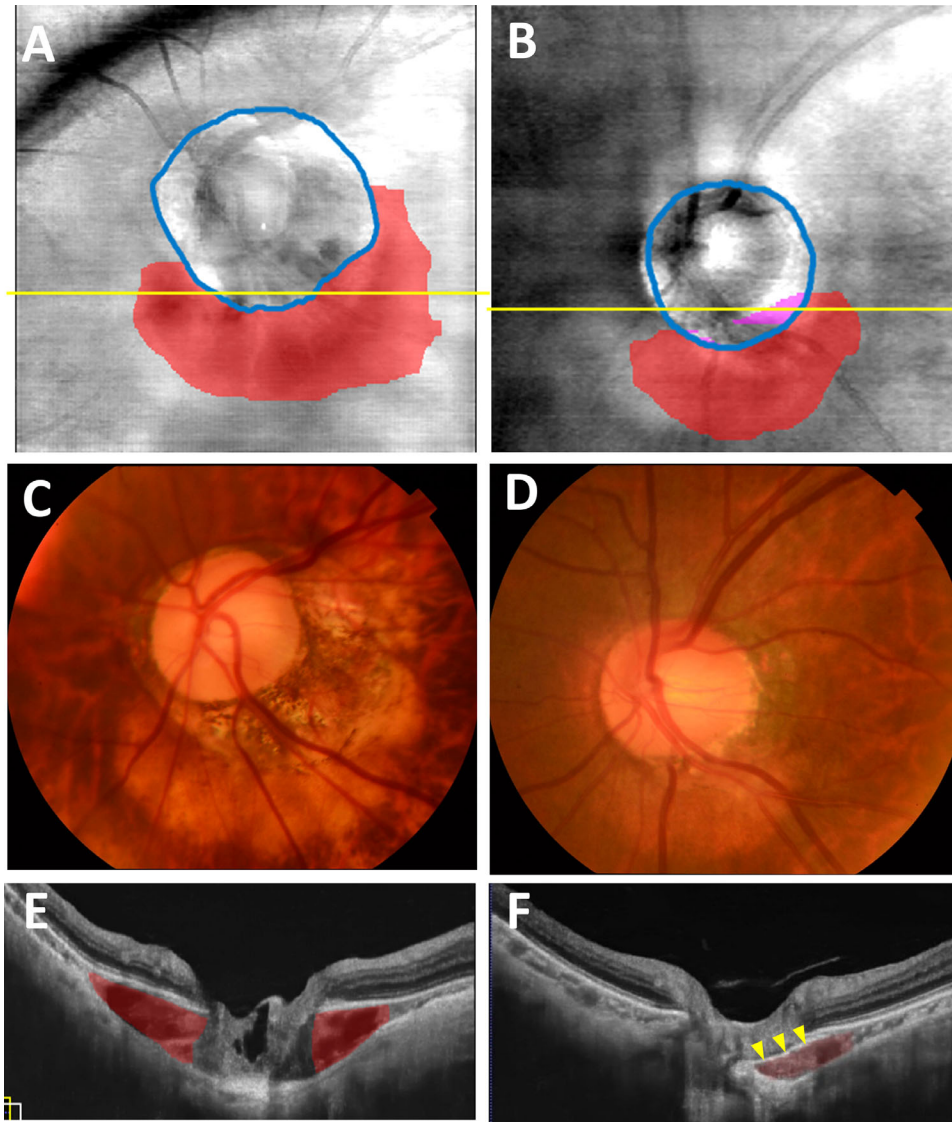
Figure 4. Representative cases of direct contact between ICCs and edges of the BMO. (A) There is no overlap in this case between the ICC and ONH. (B) A case with overlap; the *blue circles* indicate the edges of the BMO, the *red zones* indicate the ICC zones, the *pink zone* indicates the ICC–ONH overlay zone, and the *yellow lines* indicate slices of the OCT scans. (C) The disc photograph in (A). (D) The disc photograph in (B). (E) The OCT B-scan image of the *yellow line* in (A). (F) The OCT B-scan image of the *yellow line* in (B); the *yellow arrowheads* indicate the tissue of Jacoby. The ONH and ICC are separated by the tissue of Jacoby.

are shown in Figure 4. At the overlay zone, the optic nerve and ICC were separated by the tissue of Jacoby.

Discussion

We developed a 3D imaging scheme of ICCs that includes DL-based noise reduction of SS-OCT images, and we established the ICC volume parameter as a new 3D metric of ICCs. In addition, previously reported 2D parameters of the ICC (depth and length) were calculated successfully from the 3D images. ICC volume was correlated significantly with decreases in both VFMD and superior mean total deviation.

Three-dimensional evaluation has several potential advantages over 2D evaluation for understanding the characteristics of ICCs. First, 3D imaging is potentially more suitable for quantitative studies than 2D imaging. The volume can be measured more accurately than the 2D metrics because the true maximal depth and length might be missed if they exist between the slices.

In the current study, ICC volume was correlated negatively with VF severity, possibly indicating that the volume reflects the severity of the ICC. It has been recognized that eyes with an ICC often have VF impairment,[2,7–9] but the pathophysiologic link between ICCs and VF impairment remains unclear. A stretching retina over ICCs, especially with a retinal defect or a herniation into the ICC space,[10] might damage the corresponding course of nerve fiber and cause VF defects. The significant negative correlation between VF sensitivity and ICC volume supports the notion that VF impairment in eyes with ICC are pathologically related to the ICC and not merely coincidental. However, it remains unknown whether ICCs affect visual function by directly damaging the NFL or by indirectly increasing the risk of glaucoma. Also, another possibility is that eyes with larger ICCs showed more severe VFMD and superior mean total deviation because those eyes had more severe myopic optic neuropathy. Future longitudinal studies of the morphologic changes in the ICC in combination with the changes in the NFL thickness and VF sensitivity are necessary. Three-dimensional imaging is also more advantageous for this kind of longitudinal study than 2D imaging. To longitudinally evaluate the depth and length of the ICC, it is necessary but almost impossible to scan exactly the same locations over multiple visits. Our 3D imaging scheme may lead to easier and more accurate quantitative and longitudinal research, which may provide further insight into the functional consequences of the ICCs.

Three-dimensional imaging also provides information about the anatomic en face interrelationship between ICCs and adjacent tissues, which is useful for understanding the pathogenesis of ICCs. Several hypotheses about the pathogenesis of ICCs have been proposed. Some have argued that vitreous fluid may be the source of the intrachoroidal fluid accumulation,[26] and others have speculated that ICCs may represent gravitation of the subretinal fluid originating from the optic disc edge or the optic disc pits. Toranzo and associates[4] hypothesized that the choroid may be disconnected from the optic nerve as a result of retraction of the expanding staphyloma. Ohno-Matsui et al.[10,27] also reported that the choroidal thickening appeared to be accompanied by stretching of the border between the choroid and optic nerve—that is, the bordering tissue of Jacoby. In the current study, all ICCs were adjacent to the BMO. Two eyes had overlap between the ICCs and ONHs, and the ONHs and ICCs were separated by the tissue of Jacoby. These findings agreed with the hypothesis that ICCs result from stretching or disruption of the bordering tissue.

Further longitudinal study is warranted to confirm the hypothesis.

The current study has some limitations. It was a retrospective and cross-sectional case series, and too large ICCs protruding from the volume OCT scans were excluded in our study. Because ICCs are relatively rare complications, the sample size was small in this study. Therefore, our results may not cover the entire range of pathology of ICCs, and further investigation with larger sample sizes is necessary. For future analysis and clinical application, we would need to conquer some errors in the segmentation where we added manual inspection and correction. Over the last few years, deep learning has been a core technology in image segmentation,[14–17] and new architectures such as U-Net and generative adversarial networks have been developed for DL-based ophthalmologic image segmentation tasks.[28,29] In the near future, such manual inspection and correction in the segmentation should be conquered or DL-based 3D segmentation techniques should be developed with data science accumulation.[30]

Conclusions

This study showed that 3D images of ICCs were generated successfully and analyzed using DL-based noise reduction and image processing of SS-OCT volumetric scans. We established ICC volume as a new 3D parameter that reflects the pathological effect of ICCs on visual function. A 3D evaluation scheme potentially leads to an improved pathological understanding of ICCs.

Acknowledgments

Disclosure: **S. Fujimoto**, None; **A. Miki**, Topcon (F); **K. Maruyama**, Topcon (F); **S. Mei**, Topcon (E); **Z. Mao**, Topcon (E); **Z. Wang**, Topcon (E); **K. Chan**, Topcon (E); **K. Nishida**, Topcon (F)

References

1. Freund KB, Ciardella AP, Yannuzzi LA, et al. Peripapillary detachment in pathologic myopia. *Arch Ophthalmol*. 2003;121(2):197–204.

2. Shimada N, Ohno-Matsui K, Nishimuta A, Tokoro T, Mochizuki M. Peripapillary changes detected by optical coherence tomography in eyes with high myopia. *Ophthalmology*. 2007;114(11):2070–2076.

3. Tateno H, Takahashi K, Fukuchi T, Yamazaki Y, Sho K, Matsumura M. Choroidal schisis around the optic nerve in myopic eyes evaluated by optical coherence tomography. *Jpn J Clin Ophthalmol*. 2005;59:327–331.

4. Toranzo J, Cohen SY, Erginay A, Gaudric A. Peripapillary intrachoroidal cavitation in myopia. *Am J Ophthalmol*. 2005;140(4):731–732.

5. Choudhury F, Meuer SM, Klein R, et al. Prevalence and characteristics of myopic degeneration in an adult Chinese American population: the Chinese American Eye Study. *Am J Ophthalmol*. 2018;187:34–42.

6. You QS, Peng XY, Chen CX, Xu L, Jonas JB. Peripapillary intrachoroidal cavitations. The Beijing Eye Study. *PLoS One*. 2013;8(10):e78743.

7. Yeh SI, Chang WC, Wu CH, et al. Characteristics of peripapillary choroidal cavitation detected by optical coherence tomography. *Ophthalmology*. 2013;120(3):544–552.

8. Shimada N, Ohno-Matsui K, Yoshida T, et al. Characteristics of peripapillary detachment in pathologic myopia. *Arch Ophthalmol*. 2006;124(1):46–52.

9. Xie S, Kamoi K, Igarashi-Yokoi T, et al. Structural abnormalities in the papillary and peripapillary areas and corresponding visual field defects in eyes with pathologic myopia *Invest Ophthalmol Vis Sci*. 2022;63(4):13.

10. Spaide RF, Akiba M, Ohno-Matsui K. Evaluation of peripapillary intrachoroidal cavitation with swept source and enhanced depth imaging optical coherence tomography. *Retina*. 2012;32(6):1037–1044.

11. Quellec G, Charrière K, Boudi Y, Cochener B, Lamard M. Deep image mining for diabetic retinopathy screening. *Med Image Anal*. 2017;39(7):178–193.

12. Burlina P, Joshi N, Pacheco KD, Freund DE, Kong J, Bressler NM. Utility of deep learning methods for referability classification of age-related macular degeneration. *JAMA Ophthalmol*. 2018;136(11):1305–1307.

13. Bojikian KD, Lee CS, Lee AY. Finding glaucoma in color fundus photographs using deep learning. *JAMA Ophthalmol*. 2019;137(12):1361–1362.

14. Roberts PK, Vogl W-D, Gerendas BS, et al. Quantification of fluid resolution and visual acuity gain in patients with diabetic macular edema using deep learning: a post hoc analysis of a randomized clinical trial. *JAMA Ophthalmol*. 2020;138(9):945–953.

15. Moraes G, Fu DJ, Wilson M, et al. Quantitative analysis of optical coherence tomography for neovascular age-related macular degeneration using deep learning. *Ophthalmology*. 2021;128(59):693–705.

16. Loo J, Cai CX, Choong J, et al. Deep learning-based classification and segmentation of retinal cavitations on optical coherence tomography images of macular telangiectasia type 2. *Br J Ophthalmol*. 2022;106(3):396–402.

17. Kugelman J, Alonso-Caneiro D, Read SA, et al. Automatic choroidal segmentation in OCT images using supervised deep learning methods. *Sci Rep*. 2019;9(1):13298.

18. Mao Z, Miki A, Mei S, et al. Deep learning based noise reduction method for automatic 3D segmentation of the anterior of lamina cribrosa in optical coherence tomography volumetric scans. *Biomed Opt Express*. 2019;10(11):5832–5851.

19. Maruyama K, Mei S, Sakaguchi H, et al. Diagnosis of choroidal disease with deep learning-based image enhancement and volumetric quantification of optical coherence tomography. *Transl Vis Sci Technol*. 2022;11(1):22.

20. Tay E, Seah SK, Chan S-P, et al. Optic disk ovality as an index of tilt and its relationship to myopia and perimetry. *Am J Ophthalmol*. 2005;139(2):247–252.

21. Marsh-Tootle WL, Harb E, Hou W, et al. Optic nerve tilt, crescent, ovality, and torsion in a multi-ethnic cohort of young adults with and without myopia. *Invest Ophthalmol Vis Sci*. 2017;58(7):3158–3171.

22. Vianna JR, Malik R, Danthurebandara VM, et al. Beta and gamma peripapillary atrophy in myopic eyes with and without glaucoma. *Invest Ophthalmol Vis Sci*. 2016;57(7):3103–3111.

23. Yushkevich PA, Piven J, Hazlett HC, et al. User-guided 3D active contour segmentation of anatomical structures: significantly improved efficiency and reliability. *NeuroImage*. 2006;31(3):1116–1128.

24. Ohno-Matsui K, Akiba M, Moriyama M, Ishibashi T, Hirakata A, Tokoro T. Intrachoroidal cavitation in macular area of eyes with pathologic myopia. *Am J Ophthalmol*. 2012;154(2):382–393.

translational vision science & technology

25. Ohno-Matsui K, Kawasaki R, Jonas JB, et al. International photographic classification and grading system for myopic maculopathy. *Am J Ophthalmol*. 2015;159(5):877–883.

26. Wei Y-H, Yang C-M, Chen M-S, Shih Y-F, Ho T-C. Peripapillary intrachoroidal cavitation in high myopia: reappraisal. *Eye (Lond)*. 2009;23(1):141–144.

27. Ohno-Matsui K, Shimada N, Akiba M, Moriyama M, Ishibashi T, Tokoro T. Characteristics of intrachoroidal cavitation located temporal to optic disc in highly myopic eyes. *Eye (Lond)*. 2013;27(5):630–638.

28. Yoo YK, Kim BY, Jeong HK, Kim HK, Yang D, Ryu IH. Simple code implementation for deep learning-based segmentation to evaluate central serous chorioretinopathy in fundus photography. *Transl Vis Sci Technol*. 2022;11(2):22.

29. You A, Kim JK, Ryu IH, Yoo TK. Application of generative adversarial networks (GAN) for ophthalmology image domains: a survey. *Eye Vis (Lond)*. 2022;9(1):6.

30. Zarbin MA, Lee AY, Keane PA, Chiang MF. Data science in translational vision science and technology. *Transl Vis Sci Technol*. 2021;10(8):20.

Supplementary Material

Supplementary Movie S1. A representative case of 3D ICC.